Journal of Wind Engineering & Industrial Aerodynamics 225 (2022) 105005

Contents lists available at ScienceDirect

Journal of Wind Engineering & Industrial Aerodynamics

journal homepage: www.elsevier.com/locate/jweia

Study of wind loads on asphalt shingles using full-scale experimentation

Ameyu B. Tolera [a,*], Karim Mostafa [a], Arindam Gan Chowdhury [a,b], Ioannis Zisis [a,b], Peter Irwin [b]

[a] Department of Civil and Environmental Engineering, Florida International University, Miami, FL, USA
[b] Extreme Events Institute of International Hurricane Research Center, Florida International University, Miami, FL, USA

ARTICLE INFO

Keywords:
Asphalt shingles
Wind loads
Permeability
Speedup factor
Full-scale testing

ABSTRACT

Asphalt shingles constitute more than 80% of the roofing materials in current residential housing in the United States. Many post-disaster surveys have reported the failure of these roofing elements below the design level wind event. Research to realistically model the aerodynamics of asphalt shingles at full-scale is limited, resulting in knowledge gaps in peak wind loads and effects of permeability. In this study, the aerodynamics and wind resistance of asphalt shingles are studied by using a monoslope roof tested at Florida International University's Wall of Wind Experimental Facility. Results from both aerodynamic and failure assessment test protocols showed that shingles near the upper corners of the roof were subjected to high suctions due to cornering winds. This presents a critical loading case for which asphalt shingle roofing systems are not typically tested using current standard tests. Moreover, the extent of permeability underneath the shingles was observed to vary with the spatial location of shingles and wind direction. Finally, the comparison of area-averaged peak C_p values obtained from this study with GC_p plots in ASCE 7-16 Standard showed that these provisions, which do not consider the effects of permeable roofing elements (e.g., shingles), can underestimate wind loads on asphalt shingles.

1. Introduction

Over the past four decades, hurricane wind events have been responsible for numerous major disasters in the United States. The National Oceanic and Atmospheric Administration's (NOAA) Office for Coastal Management reported that the insured losses due to hurricane wind events in the U.S. between 1986 and 2015 were more than USD 515 billion. Just in 2017, the insured losses for hurricanes Harvey, Irma, and Maria were more than USD 92 billion. The total cost sustained from these hurricanes was approximately $265 Billion, with hurricane Harvey alone causing damage of more than USD 125 billion (FEMA, 2018, 2019; NOAA, 2019).

Previous wind engineering studies have conclusively shown that the bluff body aerodynamics and even the overall wind resistance of low-rise buildings are mainly dictated by the roof properties (Krishna, 1995; Stathopoulos, 1984; Uematsu and Isyumov, 1999). The damage sustained by the roof can be a global failure, whereby the whole roof truss is lifted, or a local failure of roofing elements such as shingles, tiles, or pavers. No matter how insignificant a local failure of roofing elements may seem, a roof breach would lead to water intrusion, as extreme wind events are usually accompanied by heavy rain. Many post-disaster surveys confirmed that major insured losses in residential buildings due to wind events were results of the failure of roofing elements and subsequent water intrusion (Baheru et al., 2015; Cochran and Levitan, 1994; Gurley and Masters, 2011; van de Lindt et al., 2007). Thus, the study of the wind resistance of roof coverings and their design against any liftoff that can cause water intrusion is essential.

To this end, this paper presents an investigation of the wind resistance of asphalt shingles. It is organized as follows. Section 2 reviews previous studies on roofing shingles, discusses their limitations and notes current knowledge gaps. Section 3 presents the experimental methodology employed to study wind loads on asphalt shingles under simulated wind loads and bridge the knowledge gaps. Finally, results from this study are discussed in Section 4.

2. Previous studies on roofing shingles

The wind load on permeable roofing elements has two components: the pressure over the top surface, and the pressure within the cavity (Hazelwood, 1981). The net load responsible for their uplift is then the algebraic sum between these two components (i.e., the net pressure). That is, cavity flows could result in an increase or reduction of the net pressure, termed as pressure escalation and pressure equalization, respectively. This net load is, therefore, determined by the global

* Corresponding author. Florida International University Engineering Center, 10555 W Flagler St, Miami, FL, 33174, USA.
E-mail address: atole066@fiu.edu (A.B. Tolera).

https://doi.org/10.1016/j.jweia.2022.105005
Received 16 December 2021; Received in revised form 2 April 2022; Accepted 21 April 2022
Available online 1 May 2022

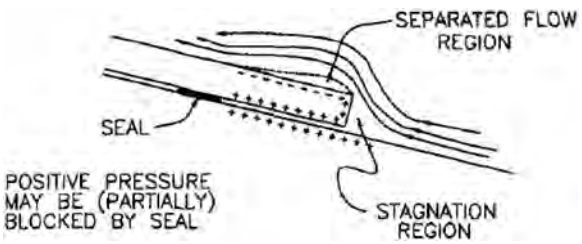

Fig. 1. Shingle liftoff mechanism (Peterka and Cermak, 1983).

building flow field, the wind gustiness, and the local element flow field (Kramer et al., 1979). Based on these fundamental notions, several studies have investigated the wind resistance of these elements (Birhane et al., 2020; Dixon et al., 2013; Habte et al., 2017; Miller et al., 2020; Mooneghi et al., 2014; Oh and Kopp, 2015; Peterka et al., 1997). This paper focuses on the wind resistance of asphalt shingles. Among roofing elements in the U.S., asphalt shingles constitute more than 80% of the roofing materials in current residential housing in the United States, as they provide the cheapest roofing solution (Dixon, 2013). Therefore, investigation of their wind performance provides a critical input towards the resilience of the built environment to wind loads. In this paper a detailed discussion is presented hereafter on the works that led up to the current shingle testing standards.

The wind resistance study of asphalt shingles started in the late 1950s. Before this time, wind engineering research on low-rise buildings was mainly focused on global aerodynamics, and not the localized wind effects on roofing elements as small as asphalt shingles (Stathopoulos, 1984). Cullen (1960) performed the study which led to the development of the first standardized wind performance test for asphalt shingles. This test was first adopted by Asphalt Roofing Industry Bureau and was later adopted with modifications by the Underwriters' Laboratories, in a document entitled UL 997 Wind Resistance of Prepared Roof Covering Materials (997) (Benjamin and Bono, 1967; Dixon et al., 2013). The testing procedures involved impinging a jet of air, from a close range at a constant speed of 26.82 m/s (60 mph) for 2 h, directly onto a shingled panel set on a typical roof slope. The target of this standard focused on testing the strength of the bituminous adhesive of self-sealing shingles. This procedure is still in use by the American Society for Testing and Materials (ASTM) Standard Test Method for Wind Resistance of Steep Slope Roofing Products (Fan-Induced Method), designated as D3161/D3161M, with modifications based on testing wind speed (ASTM International, 2020a) to account for various classes of products. This procedure fails to accurately model natural wind flows over shingled surfaces. The lack of consistency in the wind resistance of asphalt shingles in extreme wind events had been attributed to this testing method (Dixon et al., 2013).

A standardized test method was later developed by simulating atmospheric boundary layer flows in the wind tunnel for determining the wind uplift forces generated on these roofing systems (Derickson et al., 1993; Peterka et al., 1983; Peterka and Cermak, 1983). This work was motivated by the earlier lack of quantitative relationship between the turbulence properties of oncoming flow, the geometric properties of the buildings, and the associated aerodynamics. A shingled test panel with a standard three-tab seal was immersed in a turbulent flow. Blow-off tests were performed for wind directions at 0 and 45° with respect to a side of the panel, under wind speeds ranging from 13.41 m/s (30 mph) to 35.77 m/s (80 mph). The test led to the identification of a typical separation bubble over the asphalt shingles. That is, the oncoming flow would stagnate on the leading edge where it separates to cause a suction over the top surface and a positive pressure within the cavity, leading to pressure escalation. Fig. 1 shows this lift-off mechanism for asphalt shingles. Similarly, these studies showed mean pressure coefficients of 0.4 between the stagnation region and the sealing strip, and 0.2 between the sealing strip and the end of the tile opposite to the stagnation region. Moreover, following a static pressure test aimed at measuring pressure equalization, it was determined that pressure change on the top surface will almost instantly be countered by an opposite pressure change on the bottom surface, and the net pressure would be reduced significantly. Accordingly, it was concluded that uplift loads on shingles are not due to

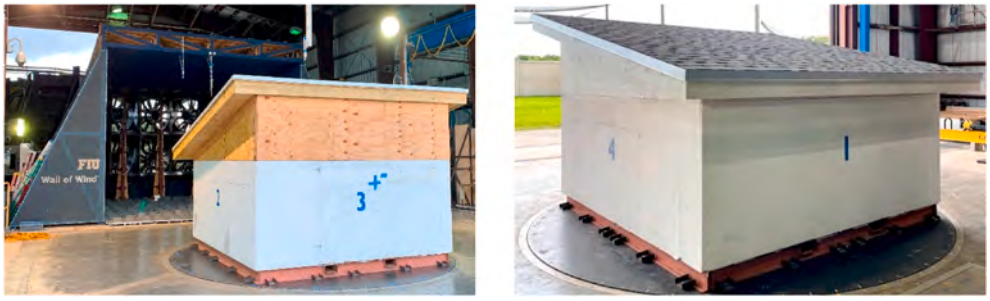

Fig. 2. Monoslope roof constructed at the WOW, FIU.

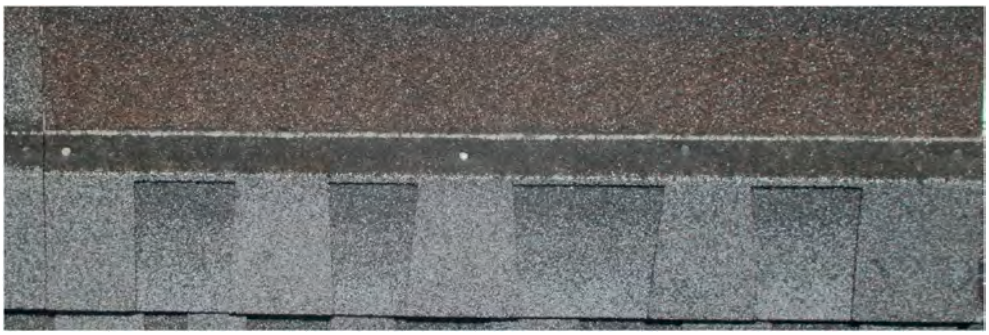

Fig. 3. A typical asphalt shingle layout.

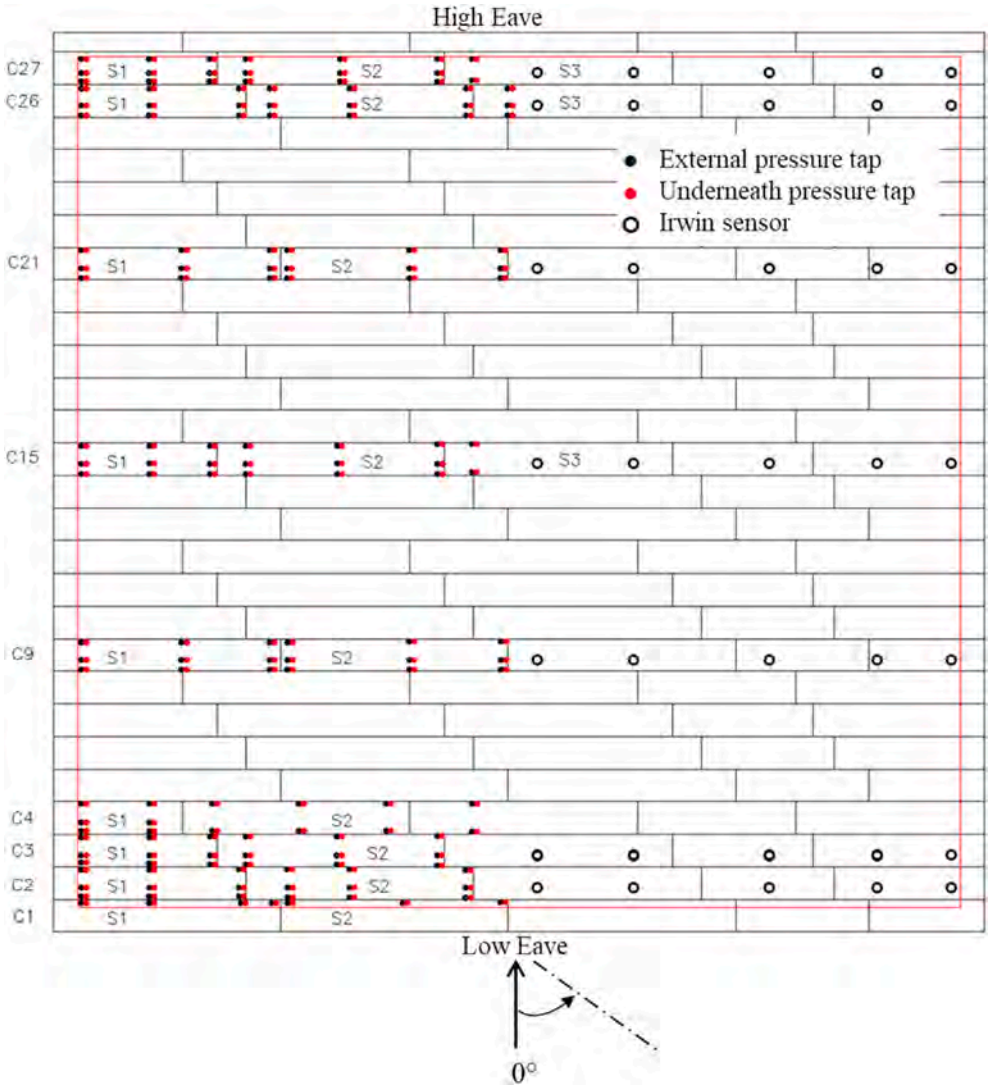

Fig. 4. Instrumentation layout for the monoslope.

pressure over the roof surface, but rather to the separated flow mechanism described earlier which, if of sufficient magnitude, could cause shingle uplift.

From these observations and a series of experiments, an analytical model based on the quasi-steady assumption was developed to relate net pressure fluctuations to the square of the local velocity fluctuations, see Eq. (1) (Derickson et al., 1993; Peterka et al., 1997).

$$D\widehat{P} = \frac{1}{2}\rho\overline{U}_{ref}^{2}\left(\frac{\widehat{U}_{roof}}{\overline{U}_{ref}}\right)^{2} D\overline{C}_{p} \tag{1}$$

where $D\widehat{P}$ is the peak net uplift pressure on the shingle, $D\overline{C}_p$ is the mean net pressure coefficient, $\widehat{U}_{roof}$ is the peak near-surface wind speed, $\overline{U}_{ref}$ is the reference mean wind speed, and ρ is the air density taken as 1.23 kg/m^3.

The validity of this assumption was supported by the fact that the evolutions in time of the near-surface velocity and pressure fluctuations are similar and that the peak-to-mean ratios for both signals are in reasonable agreement after the application of proper filters. It was subsequently found that the upper bound for the near-surface peak-to-mean ratio was 2.5 (Cochran et al., 1999). This testing procedure and analytical model were adopted by ASTM's Standard Test Method for Wind Resistance of Asphalt Shingles (Uplift Force/Uplift Resistance Method), designated as D7158/D7158M (ASTM International, 2020b). As opposed to D3161, D7158 models turbulence effects using roughness blocks placed between the fan and the testing deck, and grids on the exit end of the fans.

Dixon et al., (2013) investigated Peterka's model through full- and small-scale experiments. The small-scale experiment was conducted using Particle Image Velocimetry (PIV) to capture near-surface wind speeds using six different sloped gable-roof buildings for wind flows normal to the ridge. The results showed that the maximum speed-up factor obtained during this test was 1.69, about 30% less than the upper bound stated by Cochran et al. (1999). The full-scale test was conducted on a one-story residential house with a 6:12 sloped hip-gable bare wood roof. The highest observed speed-up factor for this case was 2.55. By overlaying the velocity signals measured from the approaching and near roof surface flow, the quasi-steady assumption was validated.

2.1. Limitation of previous works and knowledge gaps

Previous studies provided the essential start of asphalt shingle studies and have laid the fundamental procedural layout for assessing their wind resistance. However, a knowledge gap concerning peak wind

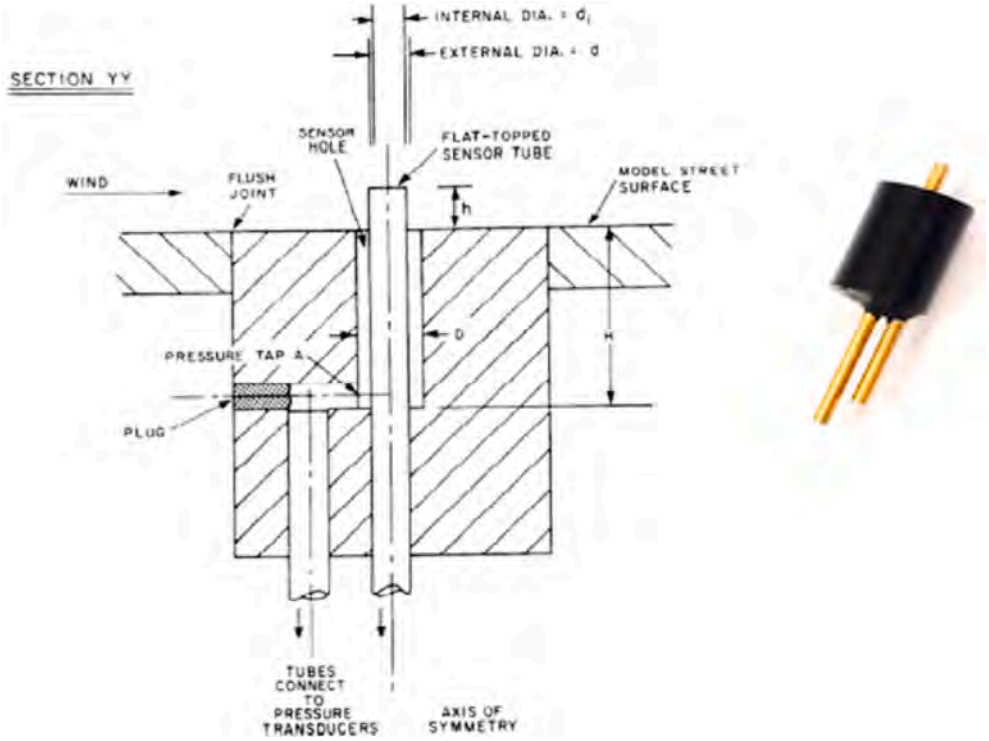

Fig. 5. Irwin sensor used for velocity measurements (Irwin, 1981).

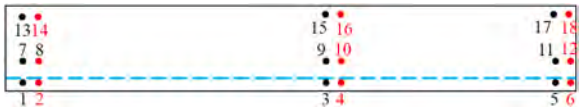

Fig. 6. Distribution of pressure taps on a typical shingle (blue line signifies self-sealing strip). (For interpretation of the references to colour in this figure legend, the reader is referred to the Web version of this article.)

loads and the effects of permeability for asphalt shingles still exists. The distribution of peak external and net wind loads on shingled roof surfaces has not been fully studied. The study conducted by Peterka et al. (1997) and previous reports that contributed to it discussed a relationship between the evolutions in time of pressures and velocity but did not study or report the magnitude of peak wind loads. Also, a static vacuum test used to measure pressure equalization achieved more than 70% in pressure reduction on net pressure. According to the current state of the art, this procedure is unrealistic. Beyond this work, there has not been any discussion on the pressure equalization extent specific to asphalt shingles.

The adopted full-scale methodology for studying the aerodynamics of a shingled deck by Peterka et al. (1997) also needs to be reconsidered. Even though full-scale shingles were applied on a testing panel, the tests were still conducted at a small wind tunnel that couldn't simulate high Reynolds number corresponding to the field conditions that may affect wind-induced loading on air-permeable roof coverings, such as asphalt shingles. Similarly, using a panel to represent a low-rise building could also misrepresent the full aerodynamics around these buildings.

Table 1
Wind parameters used in the analysis.

Parameters	Prototype	Model
Turbulence intensity, I_u (%)	23.81	8.09
Turbulence length scale, L_u (m)	13.9	0.2675
Mean roof height, H_{ref} (m)	2.11	2.11
Mean wind speed, $\overline{U}_{ref}$ (m/s)	22.6	22.6

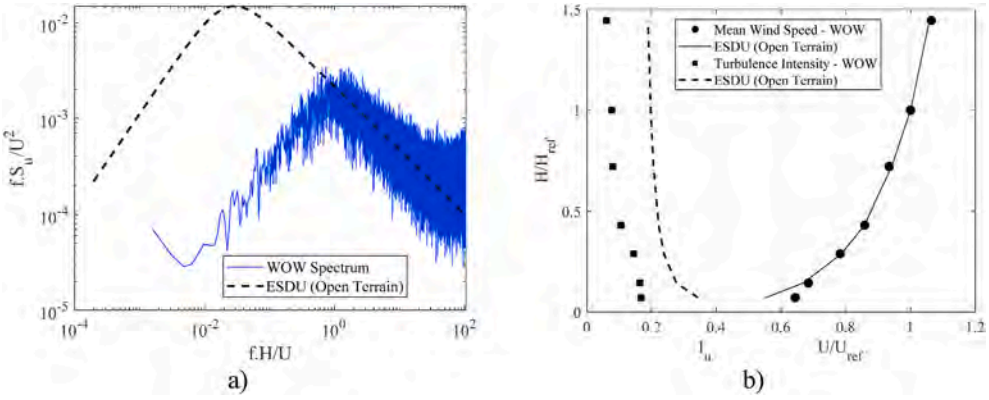

Fig. 7. (a) Von Karman and WOW wind spectra at mean roof height and (b) open terrain profile.

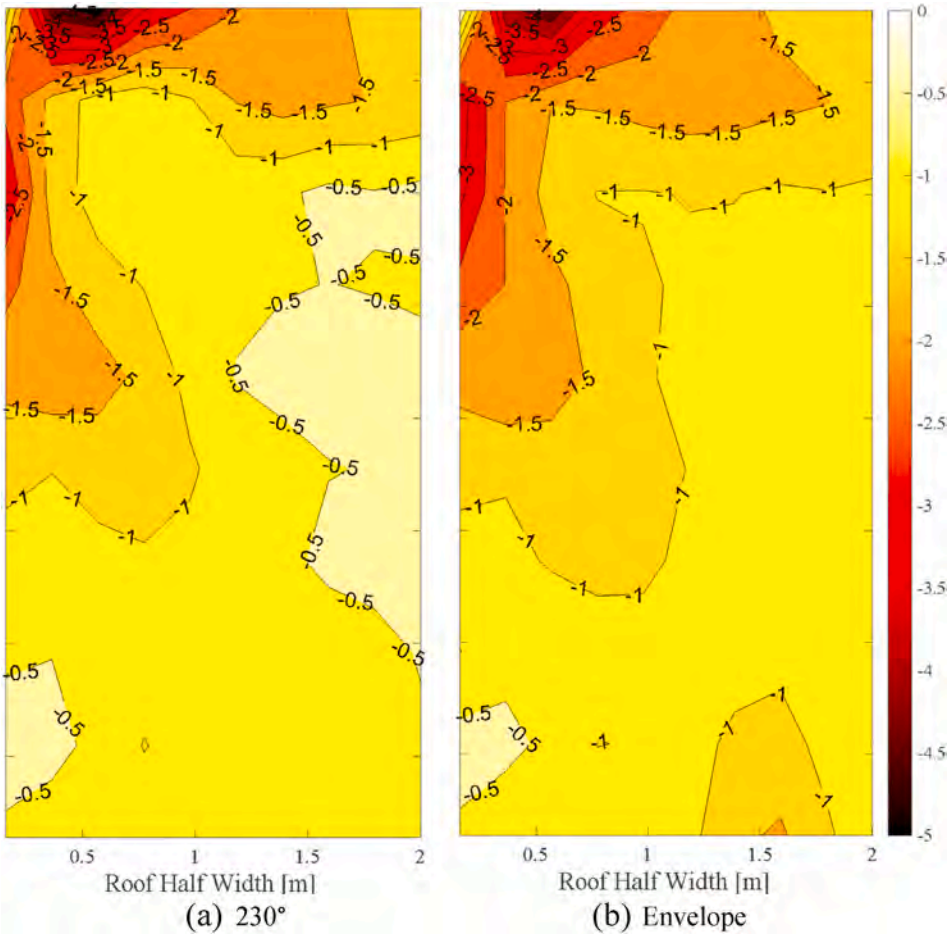

Fig. 8. $\overline{C}_{p_{ext}}$ distribution over full-scale monoslope roof for (a) 230°, and (b) envelope.

3. Experimental setup and testing protocol

Full-scale experimental tests were conducted at the 12-fan NSF-NHERI Wall of Wind (WOW) Experimental Facility (EF) at Florida International University (FIU). The WOW is a large-scale open-jet wind engineering experimental facility that can simulate the equivalent of a category 5 hurricane on the Saffir-Simpson scale with wind speeds up to 70 m/s (157 mph). The flow field of the WOW is 4.3 m high, 6.1 m wide, and 9.8 m downstream of the contraction zone, and is conditioned with spires and roughness elements that can help generate the desired atmospheric boundary layer profile (Chowdhury et al., 2017, 2018).

3.1. Roof model

For this study, a 3:12 sloped mono-slope roof with dimensions 4.1m by 3.95m was constructed at the WOW. The roof was then covered with underlayment and Miami Dade certified asphalt laminate shingles (shown in Fig. 2) by licensed roofing contractors. Each shingle was sealed to another shingle below it through self-sealing bituminous adhesive termed hereafter "sealing strip." Moreover, fasteners were used along the high end of the shingles in a row perpendicular to the roof slope to secure the shingles to the wooden roof deck. Fig. 3 shows the typical asphalt shingle that was used in this study.

3.2. Roof instrumentation

The roof was divided into two symmetrical halves, one half was instrumented with pressure taps and the other half was instrumented with Irwin sensors to record the wind pressures and near-surface wind speeds over the roof, respectively (see Fig. 4). The Irwin sensor is an omnidirectional near-surface wind speed measurement device that relates a pressure difference from its two axisymmetric pressure taps to the wind speed at a particular height above the surface, h_s (Fig. 5) This is done through two calibrated equations: Equations (2) and (3) for $h_s/h = 1.0$ and $h_s/h = 2.273$, respectively, where h is the probe height, U is the instantaneous wind speed (m/s), Δp is the instantaneous pressure difference (N/m^2), ν is the kinematic viscosity of air (taken as 14.55×10^{-6} m^2/s), and ρ is the air density (taken as 1.225 kg/m^3) (Irwin, 1981).

$$U\left(\theta,t\right) = 85\left(\frac{\nu}{h}\right) + 1.74\left(\frac{\Delta p(\theta,t)}{\rho}\right)^{0.5} \tag{2}$$

$$U\left(\theta,t\right) = 110\left(\frac{\nu}{h}\right) + 1.91\left(\frac{\Delta p(\theta,t)}{\rho}\right)^{0.5} \tag{3}$$

The roof instrumentation comprises a total of 306 pressure taps (i.e., 153 external and 153 underneath), and 35 Irwin sensors. Pressure tap installation was done simultaneously with the shingle installation to

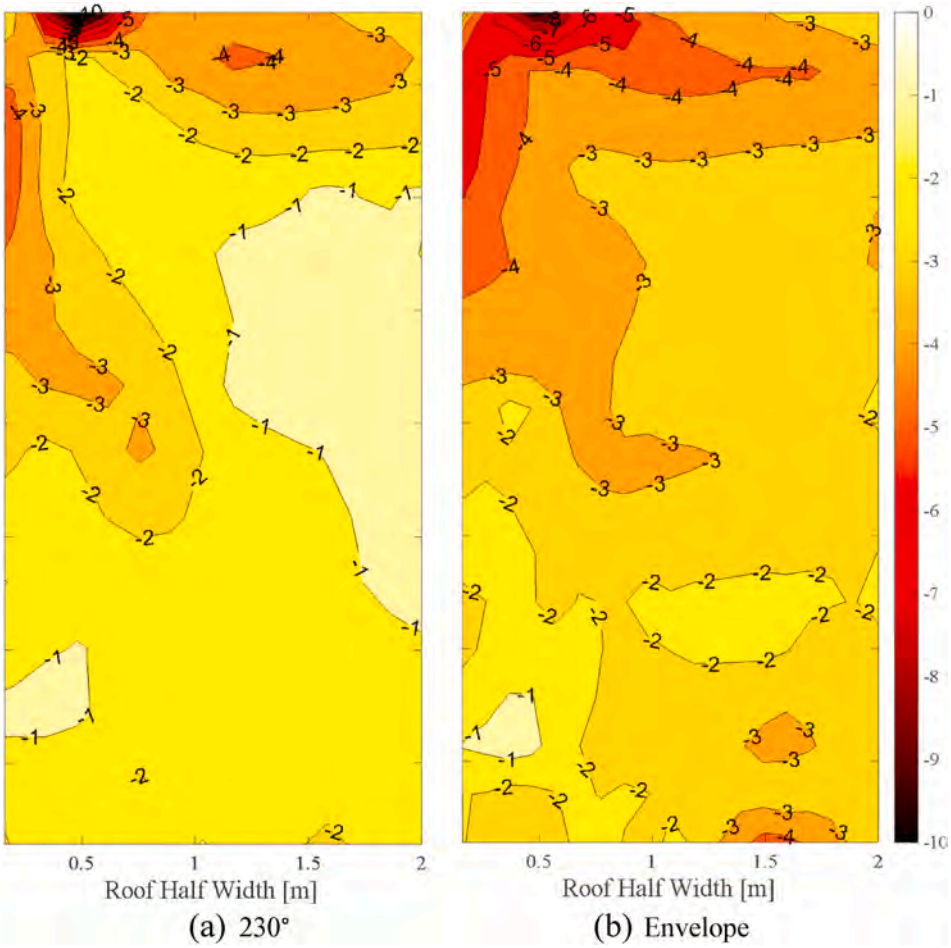

Fig. 9. $\widehat{C}_{p_{ext}}$ distribution over full-scale monoslope roof for (a) 230°, and (b) envelope.

allow their placement on the surface of both top and bottom shingle layers in the headlap region, similar to Peterka et al. (1997). On the other hand, Irwin sensors were installed after full shingle installation as they were placed flush on the top surface of the external shingles. In a typical shingle, the pressure taps were installed on three rows (i.e., one on either side of the bituminous adhesive and a third one at the upper edge of the shingle) and three columns (i.e., left, middle, and right), totaling 9 external and 9 underneath pressure taps (Fig. 6). Pressure tap numbering follows XXYYZZ format where the XX represents shingle course, YY represents shingle stand from the closer rake edge and ZZ is the tap number on an individual shingle. In this format, odd numbers pertain to external taps and even numbers represent taps underneath the shingles. Shingle course and shingle stand of instrumented sections are shown in Fig. 4. Tap 270115, for example, is the 15th tap on the 1st shingle of the 27th course.

The pressure taps and Irwin sensors were connected to Scanivalve ZOC33/DCM4000 analog scanner. The maximum pressure that could be measured by this module is 2482 Pa (0.36 psi). This pressure could be reached at speeds of about 34.1 m/s for smooth flow, and about 22.6 m/s for turbulent flow. This is the reason behind conducting the aerodynamic tests at 22.6 m/s at mean roof height, as will be further discussed in section 2.3. Tubing lengths of 1.67 m and 2.44 m were used to connect pressure taps and Irwin sensors to the pressure channels, respectively. The distortions in amplitude and phase of the measured pressures due to tubing lengths were corrected using appropriate transfer functions (Irwin et al., 1979).

3.3. Experimental testing

Aerodynamic tests were conducted at a mean wind speed of 22.6 m/s at the mean roof height (2.11 m) and an open terrain exposure of roughness height, $z_o = 0.07$m, for wind directions ranging from 0° to 360° with an increment of 10° including the cornering directions (i.e., 45°, 135°, 225°, and 315°), with a sampling time of 60 s for each direction. Fig. 7a shows the wind speed turbulence spectrum of the simulated wind flow as compared to the Von Karman spectrum, while the simulated turbulence intensity and wind speed profiles in comparison to ESDU are shown in Fig. 7b. A post-test Partial Turbulence Simulation (PTS) was performed to account for the missing low-frequency part of the spectrum (Estephan et al., 2022; Mooneghi et al., 2016; Moravej, 2018). Table 1 shows the prototype and model parameters used for PTS to compute peak pressures.

3.4. Data analysis

The pressure coefficients (C_p) were computed using Eq. (4), where ΔP is the relative differential pressure at the tap location, and $\overline{U}_{ref}$ corresponds to the mean wind speed at the mean roof height. Consequently,

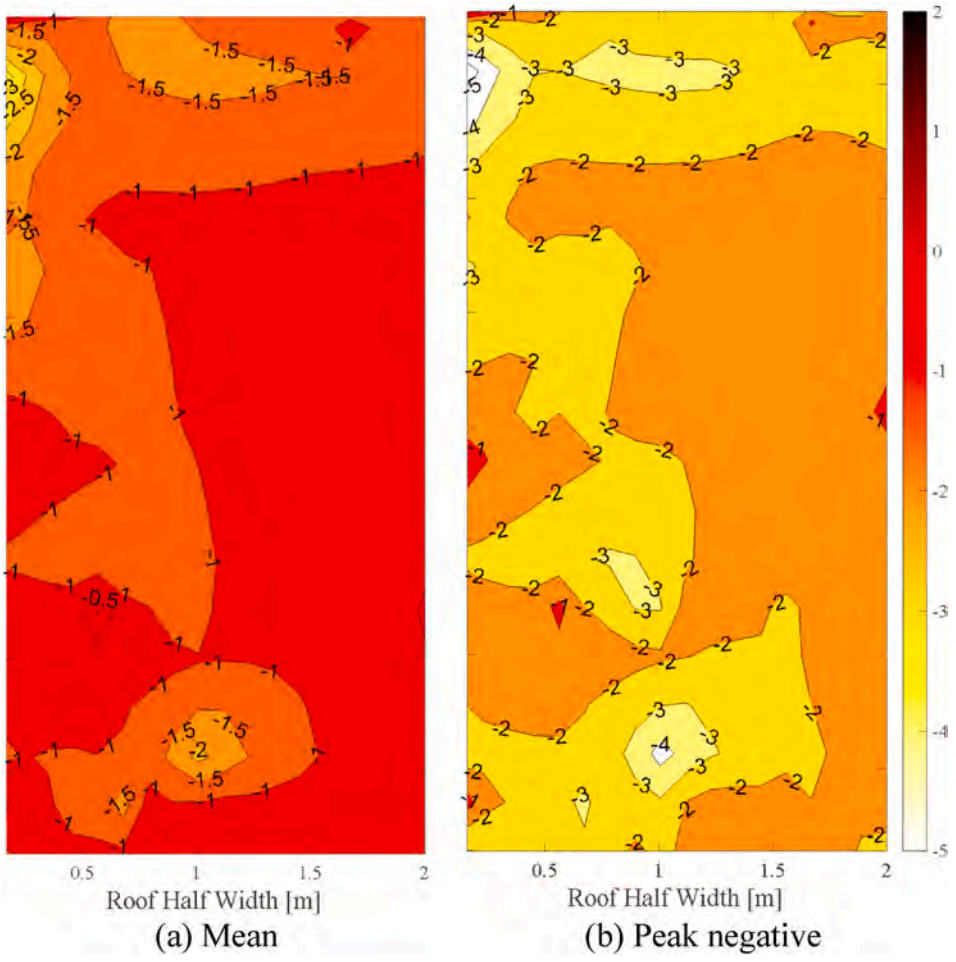

Fig. 10. $C_{p_{und}}$ envelope distribution over full-scale monoslope roof: (a) mean and (b) peak negative.

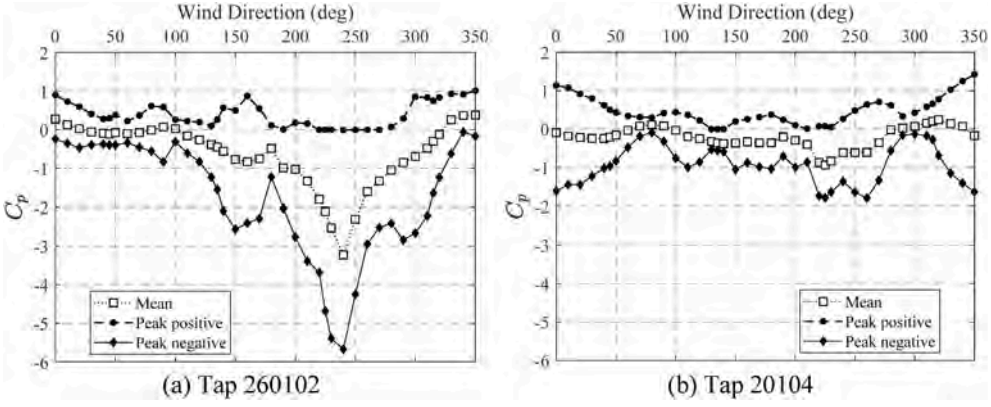

Fig. 11. Variation of $C_{p_{und}}$ with wind direction and tap location.

mean, and peak pressure coefficients (i.e., $\overline{C}_p$ and $\widehat{C}_p$) were computed as described by Eqs. (5) and (6). The PTS method was used to compensate for the missing low-frequency turbulence effects in full-scale testing. Using the PTS approach, the pressure coefficient time series were divided into N = 100 independent subintervals and $\widehat{C}_p$ were estimated based on Extreme ΔP Value distribution (i.e., Fisher Tippet Type I fit) for a 1-h storm duration. The missing low-frequency turbulence intensity was $I_{uL} = 21.7\%$, the target probability of non-exceedance was $P_N = 0.78$, and the probability of exceedance per subinterval was $G = 2.39 \times 10^{-5}$.

$$C_p(\theta,t) = \frac{\Delta P(\theta,t)}{0.5\rho\overline{U}^2_{ref}} \tag{4}$$

$$\overline{C}_p(\theta) = \frac{\overline{\Delta P}(\theta)}{0.5\rho\overline{U}^2_{ref}} \tag{5}$$

$$\widehat{C}_p(\theta) = \frac{\widehat{\Delta P}(\theta)}{0.5\rho\widehat{U}^2_{3s}} \tag{6}$$

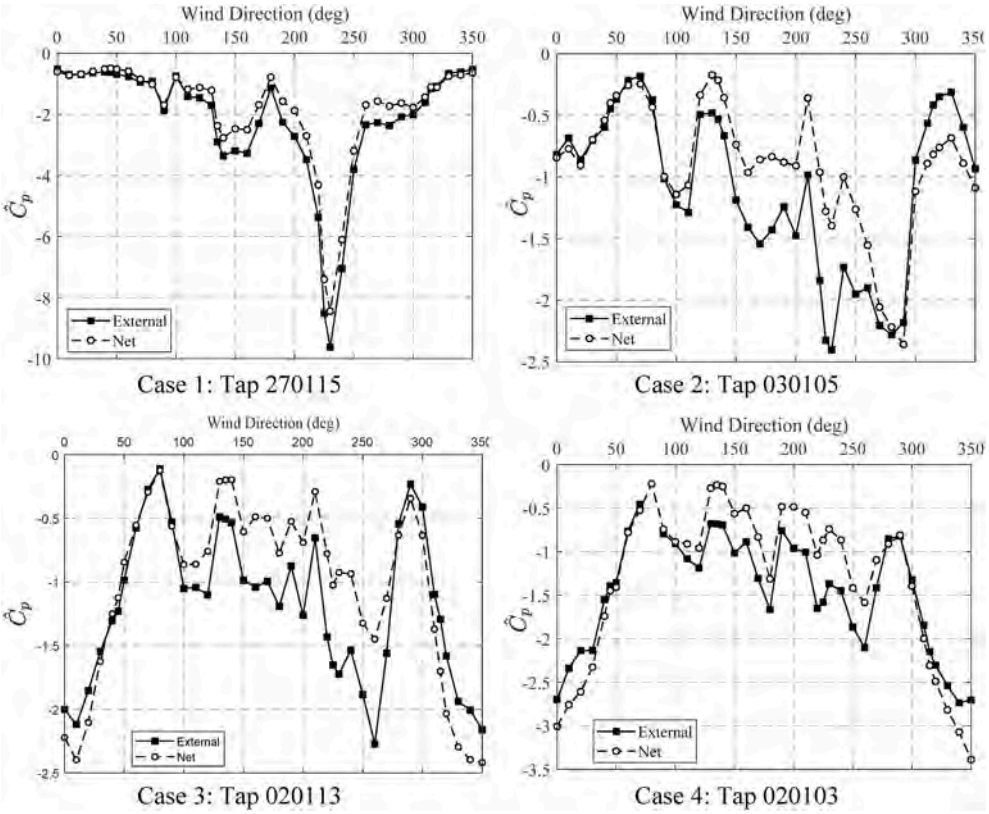

Fig. 12. Variation in $\widehat{C}_{p_{ext}}$ and $\widehat{C}_{p_{net}}$ with wind direction.

Near-surface wind speeds measured using Irwin sensors are presented in terms of a speed-up factor, $\lambda\ (\theta,\ t)$. As its name implies, this parameter relates the near-surface velocity $U_H(\theta,t)$ to the mid-roof height mean velocity $\overline{U}_{ref}$ using Eq. (7) (Cochran et al., 1999). Consequently, mean ($\overline{\lambda}$), and peak ($\widehat{\lambda}$) speed-up factors were evaluated based on their respective statistical equivalents. Eq. (8) shows the computation of the peak speed up factor $\widehat{\lambda}(\theta)$ using peak near surface velocity $\widehat{U}_H(\theta)$. Since the WOW tests were conducted in a partially simulated turbulent wind flow, the peak speed-up factor was multiplied by the reciprocal of the speed scaling factor $\lambda_U = 1.736$ (for details see Mooneghi et al. (2016)). This factor is used to compute the hourly mean wind speed from a 0.276-sec gust wind speed recorded at the WOW.

$$\lambda(\theta,t) = \frac{U_H(\theta,t)}{\overline{U}_{ref}} \tag{7}$$

$$\widehat{\lambda}(\theta) = \frac{\widehat{U}_H(\theta)}{\overline{U}_{ref}} \tag{8}$$

4. Results and discussion

4.1. Pressure coefficient results

This section presents pressure coefficients obtained in the experimental testing. The first subsection discusses pressure results from taps located at the top surfaces of external and underneath shingles, while the second subsection focuses on the net pressures.

4.1.1. External and underneath pressure coefficients

During the aerodynamic tests, cornering winds from the high-end corners of the monoslope roof were found to be critical for both surface pressures and velocities. This is consistent with previous studies on monoslope bare decks (Stathopoulos and Mohammadian, 1986) and code provisions provided for monoslope roofs such as ASCE 7-16 (ASCE, 2017). The highest external uplift pressure (i.e., suction) on the mono-slope roof was recorded for a wind direction of 230° and near the corresponding high corner. Since the pressure taps were placed on one half and the Irwin Sensors on the other, symmetrical effects are expected for the opposite halves. Therefore, similar high uplift pressures are expected to occur at the opposite high-end corner for wind directed at 130°. The minimum mean and peak pressure coefficients for these external taps were −4.99 and −9.8, respectively. Contours of the external mean and peak pressure coefficients for 230° are shown in Figs. 8 and 9. Unless otherwise stated all contour plots show only one-half of the roof, where the pressure taps were located. As discussed earlier, the other half is expected to have similar pressure distribution for symmetrical wind directions. Similarly, envelopes for minimum mean and peak pressure coefficients, $\overline{C}_p$ and $\widehat{C}_p$ respectively, (i.e., the highest in magnitude considering all wind directions) for external taps are also shown in Figs. 8 and 9. The pressure distribution from the critical wind direction and the pressure envelope are similar, showing that high pressures are mainly coming from the cornering wind directions.

While the envelope peak pressure coefficients for the external pressure taps were negative as expected, the underneath pressure taps (i.e.,

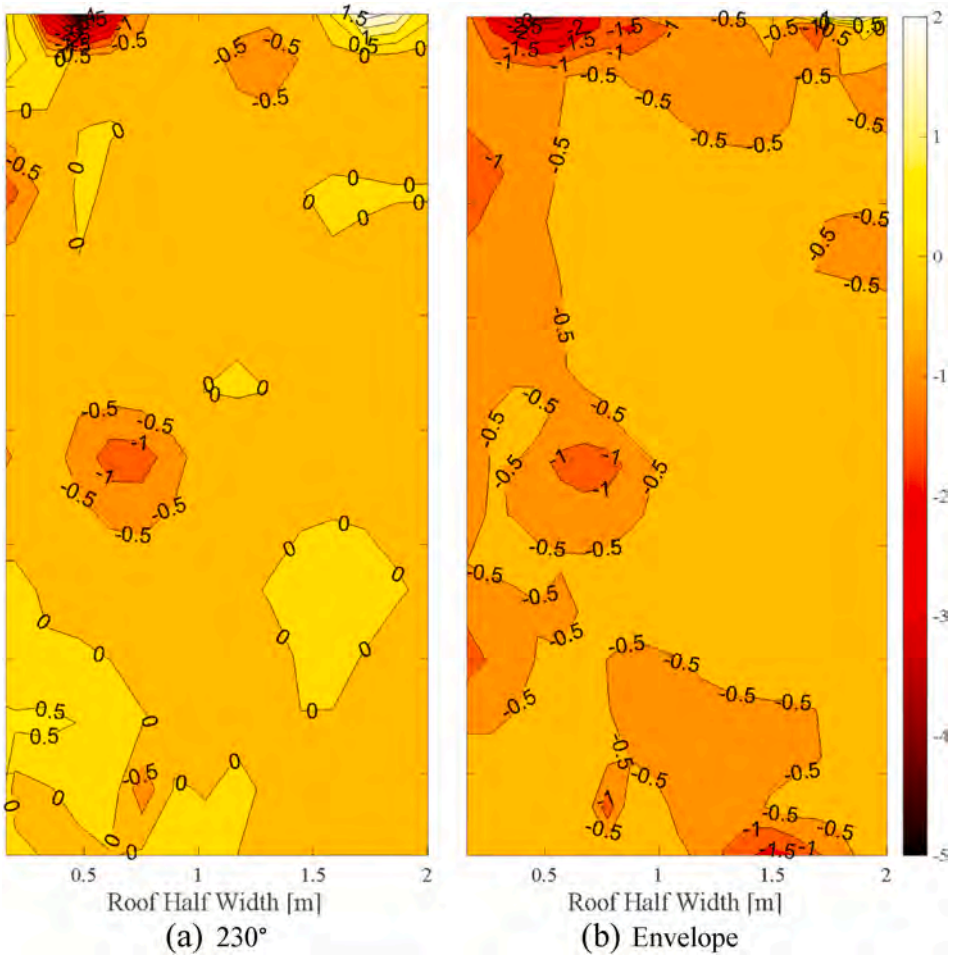

Fig. 13. $\overline{C}_{p_{net}}$ distribution over full-scale monoslope roof for (a) 230°, and (b) envelope.

within the cavity between the top and bottom shingles) had both negative and positive values. Therefore, the discussion of underneath pressures needs to specify the direction of the pressure within the cavity. Positive underneath C_p values correspond to the pressures within the cavity that are trying to lift the shingle. These pressures create a worst-case scenario when they accompany a suction on the top surface of the shingle. This phenomenon is termed pressure escalation in this paper. The opposite happens when the pressure in the cavity is negative. This pressure is adding to the adhesive force from the bituminous sealant and mechanical connections in sticking the shingles to the deck even more. As this helps reduce the overall pressure on the shingle, this phenomenon is presented as pressure equalization. The cavity pressure is, therefore, important in the determination of the net pressure on shingles, and will be further discussed in subsection 4.1.2. Though mostly negative, cavity pressures were also observed to vary with pressure tap location and wind direction. Lowest negative peak C_p values were recorded by taps located near the upper corners for oblique wind flows directed to the higher eave, similar to external pressures discussed earlier, see Fig. 10a and b. The minimum mean and peak pressure coefficients for underneath taps were $\overline{C}_p = -3.2$ and $\widehat{C}_p = \quad - \quad 5.7$, respectively, and were recorded by tap 260101 at 230° wind direction as shown in Fig. 11a. On the contrary, peak pressure coefficients ranged up to 1.5 and were measured by pressure taps located before the sealing strip for wind flows parallel to the roof slope (e.g. tap 20104 shown in Fig. 11b).

4.1.2. Net pressure and permeability factor

After the mean and peak pressure coefficients for both external and underneath taps were evaluated, the net pressure coefficients were computed as the difference between the instantaneous external and underneath pressures, see Eq. (9). This difference in pressure can also be expressed in terms of a permeability factor, $\beta(\theta)$, as shown in Eq. (10). A permeability factor value higher than 1 implies pressure escalation while a value lower than 1 indicates a pressure reduction. Note that the net pressure coefficient $C_{p\ net}(\theta, t)$ is computed using the instantaneous external and underneath pressure coefficients, $C_{p\ ext}(\theta, t)$ and $C_{p\ und}(\theta, t)$, respectively, for wind azimuth, θ.

The permeability factor, β, for codification purposes, is often computed from the absolute minimum peak external and net pressure coefficients, $\widehat{C}_{p_{ext}}(\theta)$ and $\widehat{C}_{p_{net}}(\theta)$, respectively, as in Eq. (11) (Mooneghi et al., 2015). This equation does not restrict the net and external peaks to be from the same wind direction. An alternative evaluation of β is to first calculate $\beta(\theta)$ using peaks from each wind direction, as shown in Eq. (10), and selecting the absolute maximum to look for cases where there is a possible pressure escalation. The latter method results in over-conservative β values due to consideration of insignificant net and external C_p values, which are close to 0 but still yield high β values.

$$C_{p_{net}}(\theta, t) = C_{p_{ext}}(\theta, t) - C_{p_{und}}(\theta, t) \tag{9}$$

$$\beta(\theta) = \widehat{C}_{p_{net}}(\theta) / \widehat{C}_{p_{ext}}(\theta) \tag{10}$$

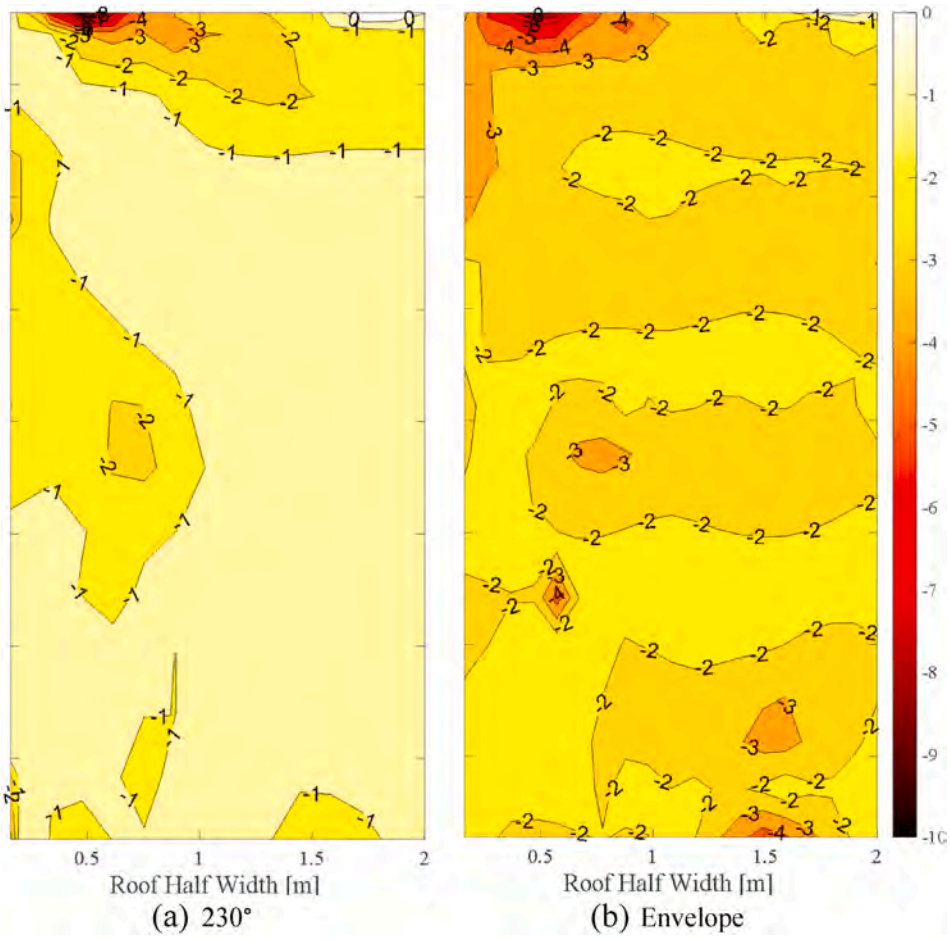

Fig. 14. $\widehat{C}_{p_{net}}$ distribution over full-scale monoslope roof for (a) 230°, and (b) envelope.

$$\beta = \min\left(\widehat{C}_{p_{net}}(\theta)\right) / \min\left(\widehat{C}_{p_{ext}}(\theta)\right) \tag{11}$$

Taking a closer look at what occurs for each wind direction, based on the value of β and the difference in azimuth for critical wind direction between the $\widehat{C}_{p_{net}}$ and $\widehat{C}_{p_{ext}}$, four different cases have been identified (see Fig. 12). The first case is where β is less than 1, and the $\min(\widehat{C}_{p_{ext}}(\theta))$ and $\min(\widehat{C}_{p_{net}}(\theta))$ are occurring in the same wind direction. In this case, we see that $\widehat{C}_{p_{net}}(\theta)$ follows a distribution similar to $\widehat{C}_{p_{ext}}(\theta)$. In the second case, β is still less than 1 but the $\min(\widehat{C}_{p_{ext}}(\theta))$ and $\min(\widehat{C}_{p_{net}}(\theta))$ occur in different wind directions. Even though there was pressure equalization in the direction of $\min(\widehat{C}_{p_{ext}}(\theta))$, this was not the critical wind direction that caused the $\min(\widehat{C}_{p_{net}}(\theta))$. In the third case β is higher than 1 and the critical wind directions for peak net and external C_p values are not the same. There was significant pressure equalization in the direction of $\min(\widehat{C}_{p_{ext}}(\theta))$, as shown in Fig. 12 case 3, but the $\min(\widehat{C}_{p_{net}}(\theta))$ is still lower due to pressure escalation and occurs in a different wind direction. Finally, fourth is the case where β is higher than 1 and the worst peak external and net C_p values occur in the same direction. Here, like case 1, $\widehat{C}_{p_{net}}(\theta)$ follows similar distribution as $\widehat{C}_{p_{ext}}(\theta)$. From these results we can see that the critical wind direction for both the net and external C_p may not necessarily happen at the same wind direction for both pressure equalization and escalation cases. This is the advantage of evaluating β based on the absolute peaks as it can be applied on code provided or experimentally obtained $\widehat{C}_{p_{ext}}$.

For the full-scale monoslope roof in this study, the lowest $C_{p_{net}}$ values were also recorded in the upper corners of the monoslope roof, and they were due to cornering winds. Mean and peak minimum C_p values recorded using pressure taps were −3.8 and −8.6 and corresponded to a wind azimuth of 230°, see Figs. 13a and 14a. The envelope $C_{p_{net}}$ for the full-scale model are shown in Figs. 13b and 14b. The permeability factor for the shingled roof is observed to be below 1 for most of the roof surface, indicating pressure equalization (see Fig. 15).

4.2. Velocity results

The computed mean and peak speed-up factors at 0.004 m (4 mm) above the roof surface ranged from 0.22 to 1.43, and from 0.55 to 2.64 respectively, see Fig. 16. Comparison of mean near-surface wind speed to their approach flow counterparts showed an increase of up to 43%, while the peak near-surface wind speeds increased by up to 264%. The ranges of these two parameters are consistent with those reported by Moravej et al. (2017) for hip and gable roofs with varying heights. Previous studies used cobra probes to measure wind speeds at 0.025m above the roof surface, as this height was assumed to be the top height for the local boundary layer (Cochran et al., 1999; Dixon et al., 2013; Habte et al., 2017; Peterka et al., 1997). For comparisons with the results of those studies, speed-up factors were computed at 0.009 m (9 mm) height from the roof surface using Eq. (3) (see section 2.2) and were extrapolated using the log law, see Eq. (12). As expected, both the mean and peak speed-up factors showed an increase at 9 mm above the roof surface compared to their counterparts at 4 mm above the roof surface, see Fig. 17. Using the speed-up factors for these two heights and solving

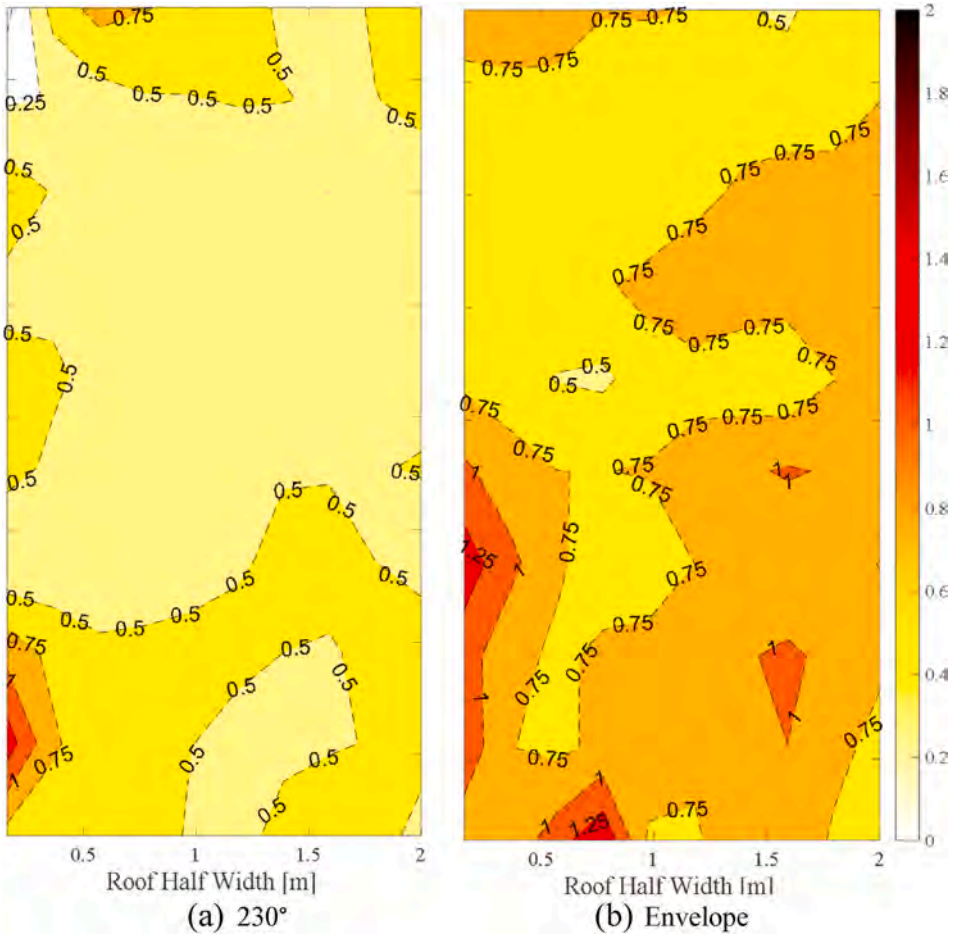

Fig. 15. (a) $\beta(230^{\circ})$ and (b) β distribution over full-scale monoslope.

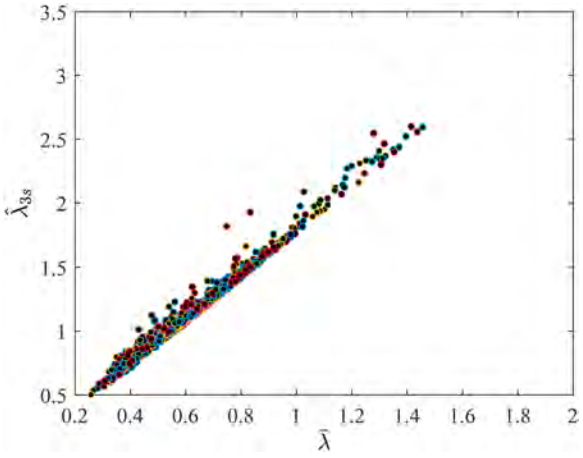

Fig. 16. $\widehat{\lambda}_{3s}$ versus $\overline{\lambda}$ at $h_s = 4$ mm.

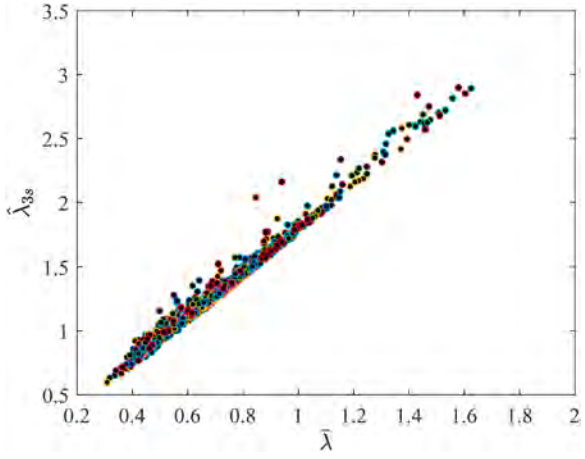

Fig. 17. $\widehat{\lambda}_{3s}$ versus $\overline{\lambda}$ at $h_s = 9$ mm.

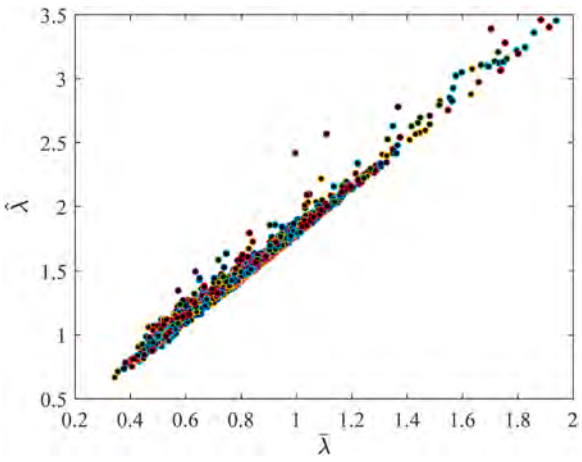

Fig. 18. $\widehat{\lambda}_{3s}$ versus $\overline{\lambda}$ at $h_s = 25$ mm.

for the mean and peak speedup factors at 25 mm, yielded approximate values of 1.9 and 3.5, respectively, see Fig. 18. The latter value is higher than an upper bound of 2.5 suggested by previous works on asphalt shingles (Cochran et al., 1999; Dixon et al., 2013; Peterka et al., 1997) but is consistent with Habte et al., (2017), who reported a maximum speedup factor of 3.2 for roofing tiles on ridges of hip-gable roofs.

$$u = \frac{u_\tau}{\kappa} \ln \frac{y}{y_o} \tag{12}$$

The near-surface wind speed-up factor and pressure coefficient distributions over the monoslope roof were found to be similar. The area of highest suction and its corresponding wind direction were found to be consistent with the area of highest speed-up factor and critical wind direction – upper corner and 230° wind direction, respectively. Figs. 19–21 show $\overline{\lambda}$ and $\widehat{\lambda}$ values at 0.004 m, 0.009 m, and 0.025 m from the surface level, respectively, for the critical wind direction of 230°. The highest peak speed-up factor at 0.025 m obtained for this wind direction was found to be 3.5. This value was also the highest value for the entire data recorded.

4.3. Failure assessment study

One of the main objectives of this study was to identify possible asphalt shingle failure modes and their relationship with pressure and velocity distributions over the roof. In this study, failure of shingles is defined as any slight shingle lift-off that would lead to the ingress of water into the building envelope. To meet this objective, a destructive test was performed at the WOW for similar flow conditions and after removing all other instrumentation. The four orthogonal and four oblique directions were selected for this test to cover all potential failure cases and were later reduced to 0°, 45°, 90°, 135°, and 180° by considering the symmetry of the monoslope roof. The testing wind speed started at 22.6 m/s 3-sec peak wind speed at mean roof height. The wind flow was maintained for 1 min in each wind direction and was increased by 4.5 m/s (10 mph) increments until failure.

Shingle vibration and liftoff were noticed along the two edges parallel to the roof slope even at 22.6 m/s during the aerodynamic testing for a cornering wind direction, see Fig. 22. But for the sake of performing the aerodynamic tests, additional nails were provided along the edges to supplement the bituminous adhesive. These nails can be seen in Fig. 23. During the failure assessment study, vibrations were once again

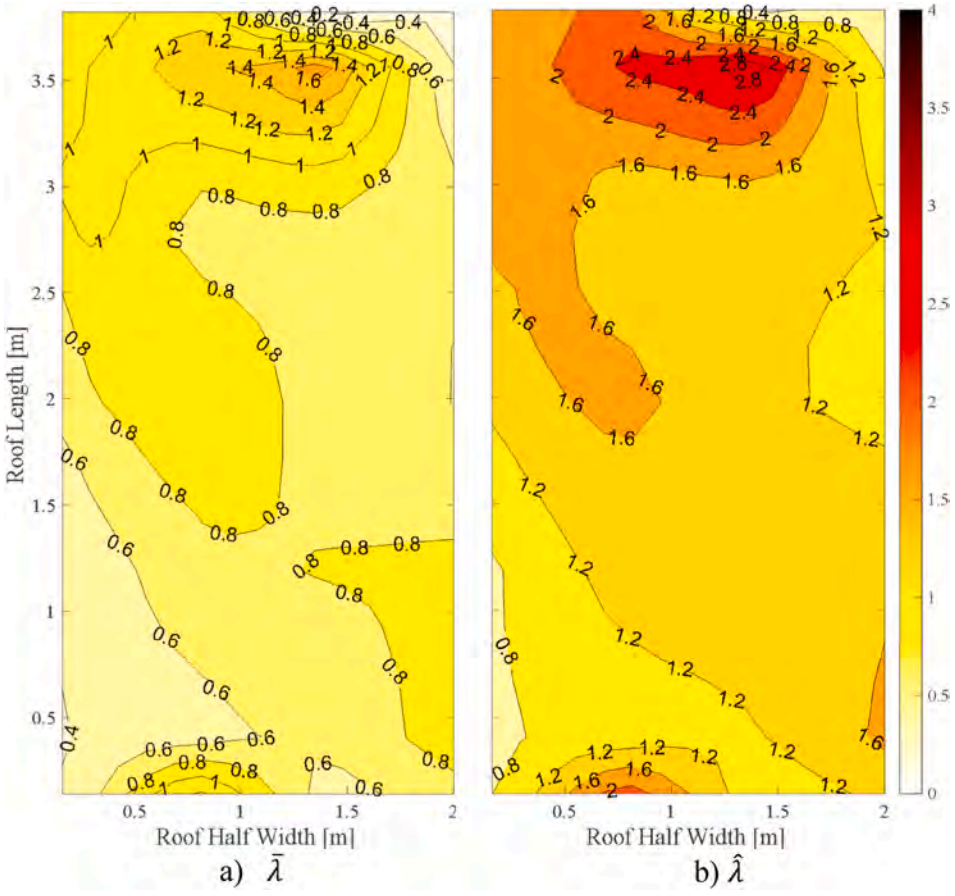

Fig. 19. (a) $\overline{\lambda}$ and (b) $\widehat{\lambda}$ contour at $h_s = 4$ mm.

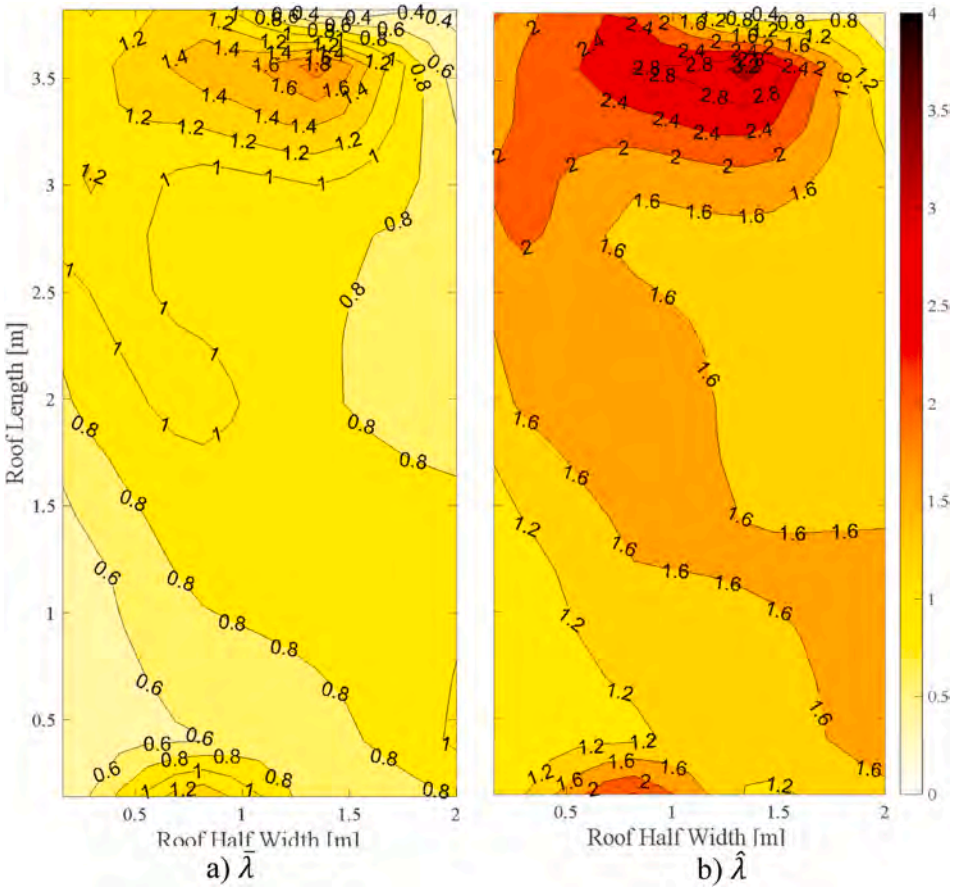

Fig. 20. (a) $\bar{\lambda}$ and (b) $\hat{\lambda}$ contour at $h_s = 9$ mm.

observed at a 3-sec peak wind speed of 33.9 m/s (76.27 mph) and increased further as the testing speed was increased.

The upper corner area of the monoslope was the most vulnerable, consistent with the observation from the aerodynamic study. Shingles in this area were blown off, most likely, due to the conical vortices from the cornering wind, at a 3-sec peak wind speed of 57 m/s (127 mph). As shown in Fig. 23, it was the shingle on the second course from the edge that initiated the failure. Once this shingle lifted, a domino effect was observed, and nearby shingles were immediately blown off. This failure mechanism is not addressed by the current shingle uplift model in use. Therefore, this presents a critical loading case for which asphalt shingles are not designed and tested.

4.4. Area-averaged pressures and codification

Studying the pressure responsible for shingle liftoff requires determining area-averaged pressure coefficients. Solely relying on peak pressure values obtained from single pressure taps may not accurately represent entire shingle areas. Asphalt shingles are installed in layers where the lower end of each shingle adheres to the one below it through a bituminous adhesive. Unless the leading edge of the upper shingle lifts first and is blown off, the bottom shingle can only lift from its lower ends. While this is the vertical placement, horizontally adjacent shingles are not connected to each other and do not share loads. Therefore, it is correct to consider the maximum area-averaging size to be a full shingle size and accordingly divide the shingle into various tap combinations. Based on previous studies on shingle failures and observed liftoff mechanisms during failure assessment study, tap combinations shown in Fig. 25 are considered for area-averaging of pressure coefficients. The tributary areas for a typical shingle are shown in Fig. 24.

The area-averaged C_p time series were computed using Eq. (13) for each wind direction by considering various tap combinations that fall in the failure initiation mechanisms discussed above. The PTS method discussed in Section 2.3 was then applied to account for the missing low-frequency component and estimate peak C_p values. Finally, the obtained values were compared to the area-averaged peak pressure coefficients (GC_p) plots provided in ASCE 7-16 for a monoslope roof with the same slope (ASCE, 2017). ASCE 7-16 provides these GC_p values for three monoslope roof zones as shown in Fig. 26. Even though the GC_p plots do not pertain to permeable roofing systems, this comparison was ideal to show their relative performance against the bare decks shown in building codes.

$$C_{p_{av}}(\theta, t) = \frac{\sum_i C_{p_i}(\theta, t) A_i}{\sum_i A_i} \tag{13}$$

For external GC_p plots, shown in Fig. 27, the area-averaged peak C_p values in all the 3 zones were seen to have significantly exceeded the plateau region provided in ASCE 7-16 due to two possible reasons. The first could be the underestimation of peak loads by ASCE 7-16. The second reason could be the difference in aerodynamics between shingled roofs compared to bare roof surfaces used for generating the ASCE 7-16 envelopes, as also reported in the literature (Habte et al., 2015; Li et al., 2014).

Comparing the net GC_p area-averaged values to the ASCE 7-16 plots showed a different phenomenon, see Fig. 28. While the net GC_p values for zones 1 and 3 were below the external GC_p plateau regions for zones 1 and 3, respectively, the zone 2 plateau region has significantly been exceeded by the net GC_p values. As opposed to the external GC_p values in

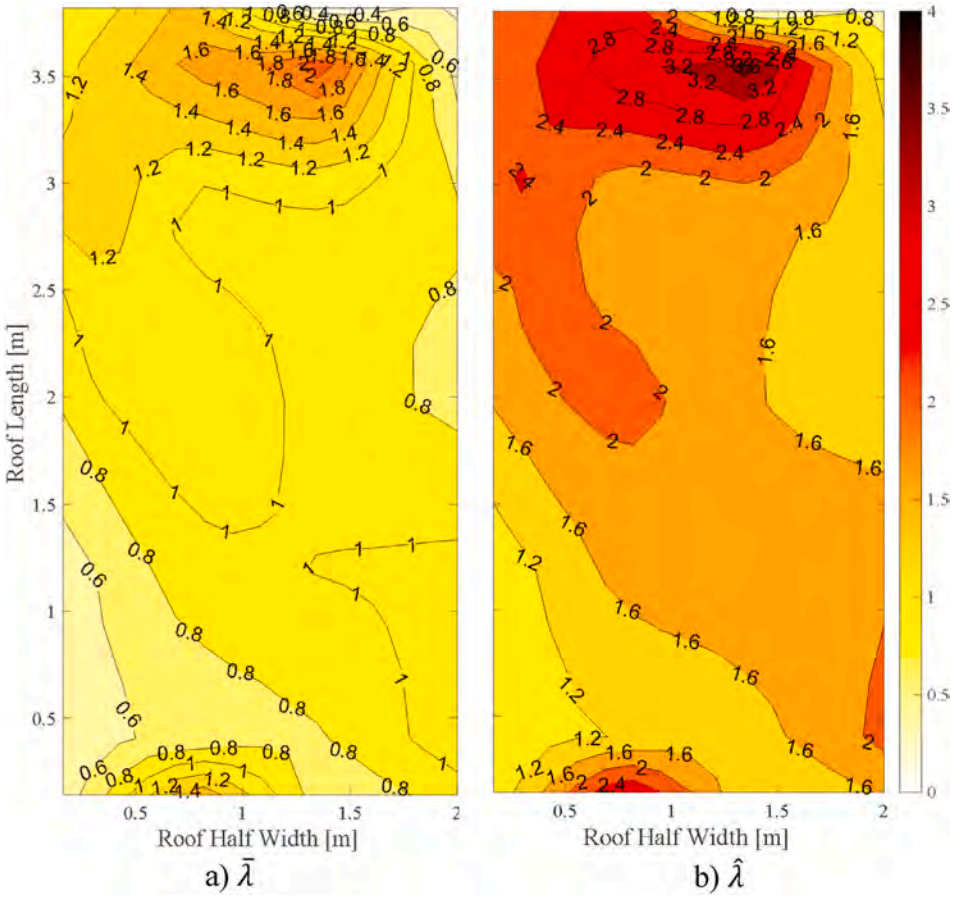

Fig. 21. (a) $\bar{\lambda}$ and (b) $\hat{\lambda}$ contour at $h_s = 25$ mm.

Fig. 22. Shingle liftoff before edge nails.

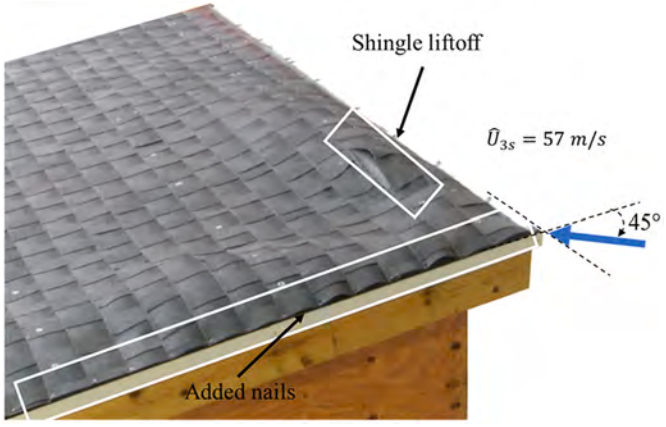

Fig. 23. Shingle liftoff before complete blowoff.

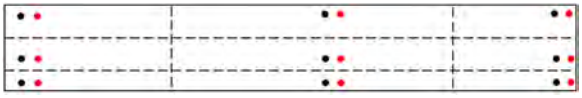

Fig. 24. Tributary areas for a typical shingle.

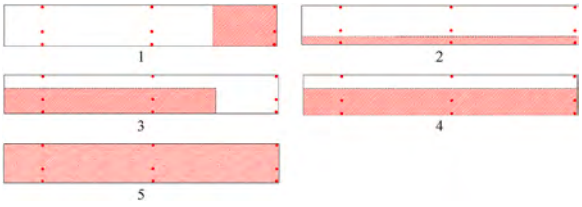

Fig. 25. Tap combinations selected for area averaging of Cp.

Fig. 27, Zone 2 and Zone 3 net GC_p values in Fig. 28 are comparable and lay under the same upper bound (i.e., $GC_p = -3$). This implies that the zonal classification of ASCE7-16 is not accurate for describing net uplift pressure distribution on asphalt shingled roofs.

Another interesting phenomenon from this study is the spatial variation of area-averaged permeability factor, β_{av}, computed from area-averaged peak external and net C_p values. Consistent with the discussions earlier, this parameter showed that there was pressure equalization for wide areas of the roof, especially zones 1 and 3 in the ASCE 7-16 provision. But some areas along the edges of the roof, (i.e., zone 2) experienced pressure escalation due to positive pressure underneath the cavity. As shown in Fig. 29 permeability factors for zone 2 are generally

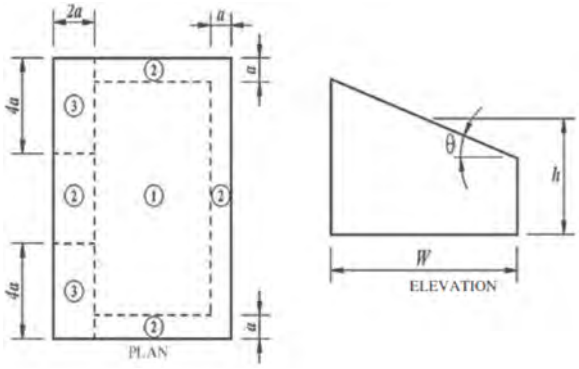

Fig. 26. ASCE 7-16 zonal classification for area-averaged peak pressure coefficients (ASCE, 2017).

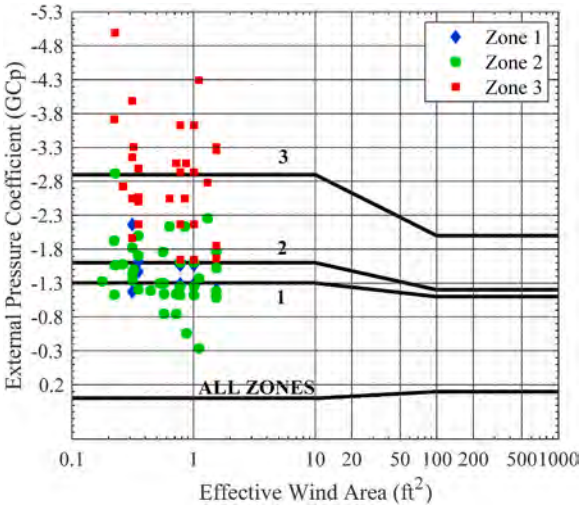

Fig. 27. Critical external pressure coefficients compared to GCp plot ASCE 7-16.

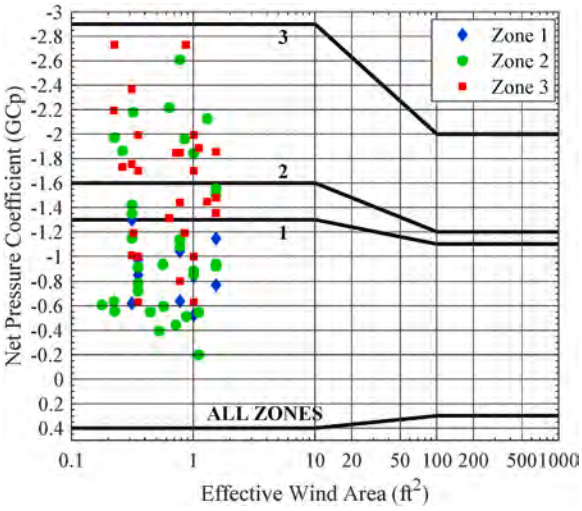

Fig. 28. Critical net pressure coefficients compared to GCp plot ASCE 7-16.

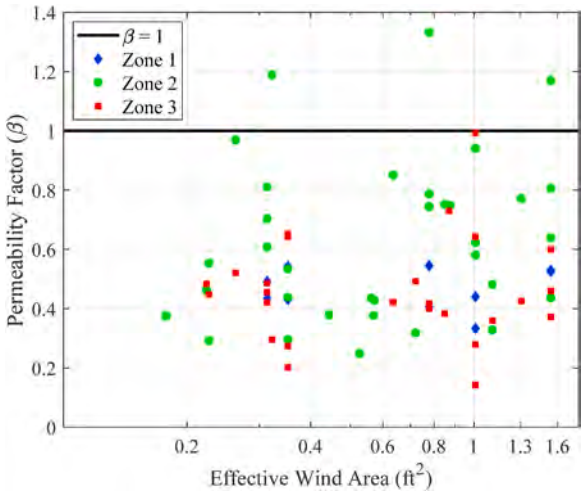

Fig. 29. Spatial variation of β according to ASCE 7-16 monoslope zones.

higher than those areas computed for zones 1 and 3.

5. Conclusions

A monoslope roof deck was used to investigate wind effects on full-scale asphalt shingles. The experimental study, performed at FIU's Wall of Wind Experimental Facility, included both aerodynamic and high-speed failure assessment tests under simulated open terrain exposure. During the aerodynamic study, pressure and velocity measurements were collected to study the distribution of aerodynamic pressure and near-surface wind speed on the roof surface. These pressures were also used to evaluate peak area-averaged C_p values for areas ranging up to a full shingle size, and for comparisons with ASCE 7-16 provisions. The failure assessment tests were conducted at wind speeds ranging from a 3-sec peak wind speed of 22.6 m/s to failure wind speeds, to identify possible failure mechanisms and their relation to aerodynamic loading and surface shear.

Both the aerodynamic and failure assessment tests showed that wind flows directed from cornering directions at the upper corners were critical. The highest suction on the roof was recorded at the upper corners of the monoslope roof at a 230° wind direction (i.e., peak external and net pressure coefficient of −9.8 and −8.6, respectively). Even though there was significant pressure equalization in this direction, the net uplift force was high enough to cause shingle uplift and blowoff. Both the peak external and net area-averaged peak pressure coefficients in these upper corners were found to exceed GC_p provisions provided in ASCE 7-16. This presents a critical loading case for which asphalt shingle roofing systems are not tested based on standard test protocols (e.g., ASTM D3161 and ASTM D7158). The results from this study showed the importance of global bluff-body aerodynamics in the loading mechanism of asphalt shingles, which is not considered by these testing standards. Moreover, envelope peak area-averaged external and net C_p values from 40 different wind directions for areas in all the three zones provided in the ASCE 7-16 were also compared with their respective external GC_p code provisions. These comparisons showed that the ASCE 7-16 provisions could underestimate wind loads on these roofing systems. Furthermore, a permeability factor, β, that relates peak external $\widehat{C}_{p_{ext}}$ values to peak net $\widehat{C}_{p_{net}}$ values was also evaluated. β was observed to be mostly less than 1, implying net pressure reduction for both individual taps and area-averaged cases. In general, β was observed to vary with shingles' spatial locations on the roof and the direction of

oncoming flow where pressure escalation cases corresponded to edge zones and wind flows into cavities.

Future research should consider the development, for various roof configurations, of a net pressure coefficients database that would complement the information on external pressure coefficient plots on bare roof surfaces provided in building standards such as ASCE 7-16. Such a database would enable designers to establish whether the net design wind load acting on any of the roof shingles is lower than the net wind load that would produce unacceptable shingle – and roof – performance.

CRediT authorship contribution statement

Ameyu B. Tolera: Conceptualization, Formal analysis, Methodology, Writing – original draft, Writing – review & editing. **Karim Mostafa:** Formal analysis, Methodology, Writing – review & editing. **Arindam Gan Chowdhury:** Conceptualization, Supervision, Resources, Funding acquisition, Writing – review & editing. **Ioannis Zisis:** Conceptualization, Supervision, Resources, Funding acquisition, Writing – review & editing. **Peter Irwin:** Conceptualization, Supervision, Validation, Writing – review & editing.

Declaration of competing interest

The authors declare that they have no known competing financial interests or personal relationships that could have appeared to influence the work reported in this paper.

Acknowledgments

This work is sponsored by the National Science Foundation (NSF) under the awards 1520853, 2037899, and IIP-1841503 (I/UCRC WHIP2019-06). The authors would also like to thank GAF for providing materials for the asphalt shingled full-scale model and technical assistance. The experiments were greatly facilitated by the fine work of WOW staff members Walter Conklin, Dr. Dejiang Chen, and Roy Liu-Marques. The authors would also like to gratefully thank RWDI for providing the Irwin Sensors used in the experiments. The opinions, findings, conclusions, or recommendations expressed in this article are solely those of the authors and do not represent the opinions of the funding agencies.

Nomenclature

Symbol	*Description*
a_{ext}	Value of a pertaining to the external shingle surface
a_{und}	Value of a pertaining to the cavity between shingles
a_{net}	Net value of a computed as an algebraic sum of external and underneath a values
$\overline{a}$	Mean value of a
$\widehat{a}$	Peak value of a
$\min(a)$	Minimum value of a
$\max(a)$	Maximum value of a
β	Permeability factor from individual taps
β_{av}	Permeability factor from area-averaged pressure coefficients
C_p	Pressure coefficient
H	Height of the low-rise building
I_u	Turbulence intensity of streamwise velocity component
L_u	Integral length scale of streamwise velocity component
ΔP	Relative differential pressure
U	Streamwise wind velocity
U_H	Streamwise wind velocity at roof height H
U_{ref}	Mean streamwise wind velocity at mean roof height
U_{3s}	Peak 3-sec streamwise wind velocity at mean roof height
z_o	Roughness length
λ	Near-surface wind speedup factor
θ	Azimuth angle of wind velocity
ρ	Density of air

References

ASCE, 2017. Minimum Design Loads and Associated Criteria for Buildings and Other Structures. American Society of Civil Engineers (ASCE), Reston, VA, USA.

ASTM International, 2020a. Standard Test Method for Wind Resistance of Steep Slope Roofing Products (Fan- Induced Method). ASTM International, West Conshohocken, PA.

ASTM International, 2020b. Standard Test Method for Wind Resistance of Asphalt Shingles (Uplift Force/Uplift Resistance Method). ASTM International, West Conshohocken.

Baheru, T., Chowdhury, A.G., Pinelli, J., 2015. Estimation of wind-driven rain intrusion through building envelope defects and breaches during tropical cyclones. Nat. Hazards Rev. 16 (2), 1–15.

Benjamin, I.A., Bono, J.A., 1967. Wind-resistance tests of roof shingles and roof assemblies. Eng. Prop. Roof. Syst. 110–29.

Birhane, T.H., Bitsuamlak, G.T., Kahsay, M.T., Awol, A.D., 2020. Air-permeability factor for wind loads on loose-laid pavers on flat roofs. J. Struct. Eng. 146 (8), 04020151.

Chowdhury, A.G., Vutukuru, K.S., Moravej, M., 2018. Full- and large-scale experimentation using the wall of wind to mitigate wind loading and rain impacts on buildings and infrastructure systems. In: Proceedings of the 11th Structural Engineering Convention (SEC18). Jadavpur University, Kolkatta, India.

Chowdhury, A.G., Zisis, I., Irwin, P., Bitsuamlak, G., Pinelli, J.P., Hajra, B., Moravej, M., 2017. Large-scale experimentation using the 12-fan wall of wind to assess and mitigate hurricane wind and rain impacts on buildings and infrastructure systems. J. Struct. Eng. 143 (7), 1–16.

Cochran, L., Levitan, M., 1994. Lessons from hurricane andrew. Architect. Sci. Rev. 37 (3), 115–121.

Cochran, L., Peterka, J., Derickson, R., 1999. Roof surface wind speed distributions on low-rise buildings roof surface wind speed distributions on low-rise buildings. Architect. Sci. Rev. 42 (3), 151–160.

Cullen, W, 1960. Wind resistance of asphalt shingle roofing. Fall Conferences of the Building Research Institute 33–42.

Derickson, R.G., Peterka, J.A., Cermak, J.E., Cochran, L.S., 1993. Wind-tunnel Study of Shingles on a Roof. Fort Collins.

Dixon, C.R., 2013. The Wind Resistance of Asphalt Roofing Shingles. University of Florida.

Dixon, C.R., Masters, F.J., Prevatt, D.O., Gurley, K.R., 2013. Investigation of the wind resistance of asphalt shingles. Adv. Hurric. Eng. 517–527.

Estephan, J., Gan Chowdhury, A., Irwin, P., 2022. In: A New Experimental-Numerical Approach to Estimate Peak Wind Loads on Roof-Mounted Photovoltaic Systems by

Incorporating Inflow Turbulence and Dynamic Effects. Engineering Structures, p. 252.
FEMA, 2018. Mitigation Assessment Team Report: Hurricane Irma in Florida.
FEMA, 2019. Mitigation Assessment Team Report: Hurricane Harvey in Texas.
Gurley, K.R., Masters, F.J., 2011. Post-2004 hurricane field survey of residential building performance. Nat. Hazards Rev. 12 (4), 177–183.
Habte, F., Asghari Mooneghi, M., Baheru, T., Zisis, I., Chowdhury, A.G., Masters, F., Irwin, P., 2017. Wind loading on ridge, hip and perimeter roof tiles: a full-scale experimental study. In: Journal of Wind Engineering and Industrial Aerodynamics, vol. 166. Elsevier Ltd, pp. 90–105.
Habte, F., Asghari Mooneghi, M., Gan Chowdhury, A., Irwin, P., 2015. Full-scale testing to evaluate the performance of standing seam metal roofs under simulated wind loading. In: Engineering Structures, vol. 105. Elsevier Ltd, pp. 231–248.
Hazelwood, R.A., 1981. The interaction of the two principal wind forces on roof tiles. J. Wind Eng. Ind. Aerod. 8, 39–48.
Irwin, H., Cooper, K.R., Girard, R., 1979. Correction of distortion effects caused by tubing systems in measurements of fluctuating pressures. In: Journal of Wind Engineering and Industrial Aerodynamics, vol. 5. Elsevier, pp. 93–107, 1–2.
Irwin, H.P.A.H., 1981. A simple omnidirectional sensor for wind-tunnel studies of pedestrian-level winds. In: Journal of Wind Engineering and Industrial Aerodynamics, vol. 7. Elsevier, pp. 219–239, 3.
Kramer, C., Gerhardt, H.J., Kuster, H.W., 1979. On the wind-loading mechanism of roofing elements. J. Ind. Aerod. 4, 415–427.
Krishna, P., 1995. Wind loads on low rise buildings - a review. J. Wind Eng. Ind. Aerod. 54–55 (C), 383–396.
Li, R., Chowdhury, A.G., Bitsuamlak, G., Gurley, K.R., 2014. Wind effects on roofs with high-profile tiles: experimental study. J. Architect. Eng. 20 (4), 1–11.
van de Lindt, J.W., Graettinger, A., Gupta, R., Skaggs, T., Pryor, S., Fridley, K.J., 2007. Performance of wood-frame structures during hurricane Katrina. J. Perform. Constr. Facil. 21 (2), 108–116.
Miller, C.S., Kopp, G.A., Morrison, M.J., 2020. Aerodynamics of air-permeable multilayer roof cladding. In: Journal of Wind Engineering and Industrial Aerodynamics, vol. 207. Elsevier Ltd, 104409. October.
Mooneghi, M.A., Irwin, P., Chowdhury, A.G., 2014. Large-scale testing on wind uplift of roof pavers. In: Journal of Wind Engineering and Industrial Aerodynamics, vol. 128. Elsevier, pp. 22–36.
Mooneghi, M.A., Irwin, P., Chowdhury, A.G., 2015. Design guidelines for roof pavers against wind uplift. Struct. Congr. 2679–2688.
Mooneghi, M.A., Irwin, P., Chowdhury, A.G., 2016. Partial turbulence simulation method for predicting peak wind loads on small structures and building appurtenances. In: Journal of Wind Engineering and Industrial Aerodynamics, vol. 157. Elsevier, pp. 47–62.
Moravej, M., 2018. Investigating Scale Effects on Analytical Methods of Predicting Peak Wind Loads on Buildings. Florida International University.
Moravej, M., Irwin, P., Zisis, I., Chowdhury, A.G., Hajra, B., 2017. Effects of roof height on local pressure and velocity coefficients on building roofs. In: Engineering Structures, vol. 150. Elsevier Ltd, pp. 693–710.
NOAA, 2019. Hurricane Costs. National Oceanic and Atmospheric Administration. https://coast.noaa.gov/states/fast-facts/hurricane-costs.html.
Oh, J.H., Kopp, G.A., 2015. An experimental study of pressure distributions within an air-permeable, double-layer roof system in regions of separated flow. J. Wind Eng. Ind. Aerod. 138, 1–12.
Peterka, J.A., Cermak, J.E., 1983. Wind-tunnel Study of Wind Resistance of Roofing Shingles. Fort Collins.
Peterka, J.A., Cermak, J.E., Cochran, L.S., Cochran, B.C., Hosoya, N., Derickson, R.G., Harper, C., Jones, J., Metz, B., 1997. Wind uplift model for asphalt shingles. J. Architect. Eng. 3 (4), 147–155.
Peterka, J.A., Cermak, J.E., Hosoya, N., 1983. Wind-Tunnel Study of Wind Pressures on Roofing Shingles. Fort Collins.
Stathopoulos, T., 1984. Wind loads on low-rise buildings: a review of the state of the art. Eng. Struct. 6 (2), 119–135.
Stathopoulos, T., Mohammadian, A.R., 1986. Wind loads on low buildings with mono-sloped roofs. J. Wind Eng. Ind. Aerod. 23, 81–97.
Uematsu, Y., Isyumov, N., 1999. Wind pressures acting on low-rise buildings. J. Wind Eng. Ind. Aerod. 82, 1–25.